Center for Environmentally Sustainable Transportation in Cold Climates

Numerical Simulation of Snow Deposition around Living Snow Fences

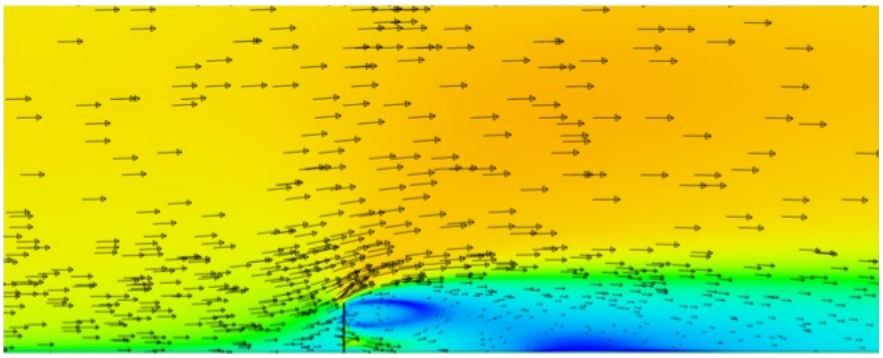

John Petrie, Assistant Professor, California State University, Los Angeles
Kun Zhang, Assistant Professor, California State University, Chico
Mahmoud Shehata, Graduate Research Assistant, Washington State University

Date: 30/08/2019

Prepared by: John Petrie

Center for Environmentally Sustainable Transportation in Cold Climates
University of Alaska Fairbanks
P.O. Box 755900
Fairbanks, AK 99775

U.S. Department of Transportation
1200 New Jersey Avenue, SE
Washington, DC 20590

INE/CESTiCC 19.17

REPORT DOCUMENTATION PAGE

Form approved OMB No.

1. AGENCY USE ONLY (LEAVE BLANK)	2. REPORT DATE	3. REPORT TYPE AND DATES COVERED
	08/2019	Final Report: 09/2016 – 08/2019

4. TITLE AND SUBTITLE

Numerical Simulation of Snow Deposition around Living Snow Fences

5. FUNDING NUMBERS

6. AUTHOR(S)
John Petrie, Assistant Professor, California State University, Los Angeles
Kun Zhang, Assistant Professor, California State University, Chico
Mahmoud Shehata, Graduate Research Assistant, Washington State University

7. PERFORMING ORGANIZATION NAME(S) AND ADDRESS(ES)

Center for Environmentally Sustainable Transportation in Cold Climates
University of Alaska Fairbanks
Duckering Building Room 245
P.O. Box 755900
Fairbanks, AK 99775-5900

8. PERFORMING ORGANIZATION REPORT NUMBER

9. SPONSORING/MONITORING AGENCY NAME(S) AND ADDRESS(ES)

U.S. Department of Transportation
1200 New Jersey Avenue, SE
Washington, DC 20590

10. SPONSORING/MONITORING AGENCY REPORT NUMBER

11. SUPPLENMENTARY NOTES

12a. DISTRIBUTION / AVAILABILITY STATEMENT

No restrictions

12b. DISTRIBUTION CODE

13. ABSTRACT (Maximum 200 words)

In this study, computational fluid dynamics (CFD) was used to investigate the air flow around porous snow fences to gain insight into snow transport and deposition in the vicinity of fences. Numerical simulations were performed to validate the CFD approach using experimental data from a wind tunnel study. Subsequent simulations were used to test the use of a porosity model to represent fence geometry and determine the effect of fence spacing for fences comprised of multiple rows. The results demonstrate that CFD simulations can reproduce the aerodynamics around porous fences. Additionally, the flow field generated with a porosity model is in close agreement with that from a model with explicit representation of fence porosity. Simulations of fences comprised of two rows spaced at various distances demonstrate that when the row spacing is small the fence behaves as a single row.

14- KEYWORDS :

snow fence, computational fluid dynamics, windbreaks, aerodynamics, snow and ice control

15. NUMBER OF PAGES

36

16. PRICE CODE

N/A

17. SECURITY CLASSIFICATION OF REPORT	18. SECURITY CLASSIFICATION OF THIS PAGE	19. SECURITY CLASSIFICATION OF ABSTRACT	20. LIMITATION OF ABSTRACT
Unclassified	Unclassified	Unclassified	N/A

NUMERICAL SIMULATION OF SNOW DEPOSITION AROUND LIVING SNOW FENCES

Final Report

by

John Petrie, California State University, Los Angeles, Assistant Professor
Kun Zhang, California State University, Chico, Assistant Professor
Mahmoud Shehata, Washington State University, Graduate Research Assistant

College of Engineering, Computer Science, and Technology
California State University, Los Angeles
5151 State University Drive
Los Angeles, CA 90032-8151

A report prepared for the
Center for Environmentally Sustainable Transportation in Cold Climates
University of Alaska Fairbanks
Duckering Building, Room 245
P.O. Box 755900
Fairbanks, AK 99775-5900

CESTiCC Project N0. 1626

August 30, 2019

DISCLAIMER

This document is disseminated under the sponsorship of the U. S. Department of Transportation in the interest of information exchange. The U.S. Government assumes no liability for the use of the information contained in this document. The U.S. Government does not endorse products or manufacturers. Trademarks or manufacturers' names appear in this report only because they are considered essential to the objective of the document.

Opinions and conclusions expressed or implied in the report are those of the author(s). They are not necessarily those of the funding agencies.

METRIC (SI*) CONVERSION FACTORS

APPROXIMATE CONVERSIONS TO SI UNITS

Symbol	When You Know	Multiply By	To Find	Symbol
		LENGTH		
in	inches	25.4		mm
ft	feet	0.3048		m
yd	yards	0.914		m
mi	Miles (statute)	1.61		km
		AREA		
in^2	square inches	645.2	millimeters squared	cm^2
ft^2	square feet	0.0929	meters squared	m^2
yd^2	square yards	0.836	meters squared	m^2
mi^2	square miles	2.59	kilometers squared	km^2
ac	acres	0.4046	hectares	ha
		MASS (weight)		
oz	Ounces (avdp)	28.35	grams	g
lb	Pounds (avdp)	0.454	kilograms	kg
T	Short tons (2000 lb)	0.907	megagrams	mg
		VOLUME		
fl oz	fluid ounces (US)	29.57	milliliters	mL
gal	Gallons (liq)	3.785	liters	liters
ft^3	cubic feet	0.0283	meters cubed	m^3
yd^3	cubic yards	0.765	meters cubed	m^3

Note: Volumes greater than 1000 L shall be shown in m^3

		TEMPERATURE (exact)		
ºF	Fahrenheit temperature	5/9 (ºF-32)	Celsius temperature	ºC
		ILLUMINATION		
fc	Foot-candles	10.76	lux	lx
fl	foot-lamberts	3.426	candela/m^2	cd/cm^2
		FORCE and PRESSURE or STRESS		
lbf	pound-force	4.45	newtons	N
psi	pound-force per square inch	6.89	kilopascals	kPa

These factors conform to the requirement of FHWA Order 5190.1A *SI is the symbol for the International System of Measurements

APPROXIMATE CONVERSIONS FROM SI UNITS

Symbol	When You Know	Multiply By	To Find	Symbol
		LENGTH		
mm	millimeters	0.039	inches	in
m	meters	3.28	feet	ft
m	meters	1.09	yards	yd
km	kilometers	0.621	Miles (statute)	mi
		AREA		
mm^2	millimeters squared	0.0016	square inches	in^2 m^2
meters squared		10.764	square feet	ft^2 km^2
kilometers squared		0.39	square miles	mi^2 ha
hectares (10,000 m^2)		2.471	acres	ac
		MASS (weight)		
g	grams	0.0353	Ounces (avdp)	oz
kg	kilograms	2.205	Pounds (avdp)	lb mg
megagrams (1000 kg)		1.103	short tons	T
		VOLUME		
mL	milliliters	0.034	fluid ounces (US)	fl oz
liters	liters	0.264	Gallons (liq)	gal
m^3	meters cubed	35.315	cubic feet	ft^3
m^3	meters cubed	1.308	cubic yards	yd^3

		TEMPERATURE (exact)		
ºC	Celsius temperature	9/5 ºC+32	Fahrenheit temperature	ºF
		ILLUMINATION		
lx	lux	0.0929	foot-candles	fc
cd/cm^2	candela/m^2	0.2919	foot-lamberts	fl
		FORCE and PRESSURE or STRESS		
N	newtons	0.225	pound-force	lbf
kPa	kilopascals	0.145	pound-force per square inch	psi

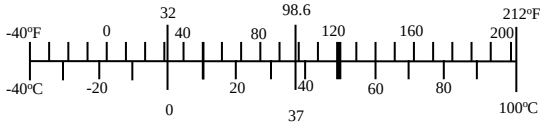

ACKNOWLEDGEMENTS

The authors would like to thank Flow Science, Inc. (Santa Fe, NM) for providing access to the Flow-3D software.

TABLE OF CONTENTS

LIST OF FIGURES

EXECUTIVE SUMMARY

Maintaining safe highway conditions through measures that are both economically and environmentally sustainable remains a challenge in cold regions. Blowing snow and snow drifts covering the road create unsafe driving conditions that can result in loss of life and adverse economic consequences. Traditional mitigation strategies include plowing and/or salting roadways. While effective, these solutions are often prohibitively expensive and produce negative environmental impacts. When properly designed, the use of snow fences is an effective and economic solution to the problems of snowdrift on roads and blowing snow above roads. A structural snow fence, which is manufactured from wood, plastic, or metal, can be placed adjacent to the highway to disrupt snow transport and encourage deposition away from the road. Alternatively, living snow fences (LSFs), which are comprised of some combination of trees, shrubs, and grasses, have been identified as a cost-effective and environmentally sustainable solution to mitigate hazardous driving conditions. Additional benefits may be derived from LSFs such as providing carbon sequestration, enhancing wildlife habitat, improving erosion control and water quality, reducing flooding, as well as maintaining a more natural appearance to the landscape.

In this study, computational fluid dynamics (CFD) was used to investigate the air flow around snow fences to gain insight into snow transport in the vicinity of fences. Numerical simulations were performed to validate the CFD approach using experimental data from a wind tunnel study. Subsequent simulations were used to test the use of a porosity model to represent fence geometry and determine the effect of fence spacing for fences comprised of multiple rows. Simulations were performed using the Flow-3D CFD software.

Major findings of this study include:

- Computational fluid dynamics (CFD) simulations can reproduce aerodynamic properties, such as the velocity distribution, around porous fences.
- For structural fences with regular geometry, the fence can be incorporated directly into the model as part of the geometry. For living snow fences with irregular geometry, the true fence geometry is difficult to represent directly in the model. Instead, a porosity model can be implemented to model the effect of the porous fence on the flow.
- Living snow fences comprised of two rows of vegetation with a row spacing of less than about 5*H*, where *H* = fence height, produce the same effects as a snow fence with a single row of vegetation. Larger row spacing requires consideration of both rows of vegetation.

Recommendations following from these findings are that:

- Work is needed to provide recommendations for appropriate use of the Darcy-Forchheimer equation with LSFs. In particular, guidance on the selection of appropriate drag coefficients for different species is needed. Ideally, this work would include data from wind tunnel experiments to validate numerical models.
- Monitoring of LSF field sites is needed to provide quantitative data on performance and inform numerical models. The collected data should include, at a minimum, fence geometry and topography, wind speed and direction, as well as measurements of blown snow and snow deposition.
- Further work is needed to incorporate the snow transport process into CFD models. Possible approaches include a Lagrangian particle transport model or an Eulerian multiphase fluid model. These models can be used to correlate snow transport with aerodynamic characteristics to clarify the snow transport mechanisms around porous fences.

CHAPTER 1. INTRODUCTION

Maintaining safe highway conditions through measures that are both economically and environmentally sustainable remains a challenge in cold regions. Blowing snow and snow drifts covering the road create unsafe driving conditions that can result in loss of life and economic consequences including increased travel times and damage to pavement. Traditional mitigation strategies include plowing and/or salting roadways. While effective, these solutions are often prohibitively expensive and produce negative environmental impacts. When properly designed, snow fences are an effective and economic solution to the problems of snowdrift on roads and blowing snow above roads (Tabler and Meena, 2006). A snow fence, as shown in Figure 1a, is a structural fence manufactured from wood, plastic, or metal placed adjacent to the highway to disrupt snow transport and encourage deposition away from the road. Living snow fences (LSFs) have been identified as another cost-effective and environmentally sustainable solution to mitigate hazardous driving conditions (Wyatt et al., 2012). LSFs, such as the example shown in Figure 1b, are composed of some combination of trees, shrubs, and grasses. Additional benefits derived from LSFs include providing carbon sequestration, enhancing wildlife habitat, improving erosion control and water quality, reducing flooding, as well as maintaining a more natural appearance to the landscape.

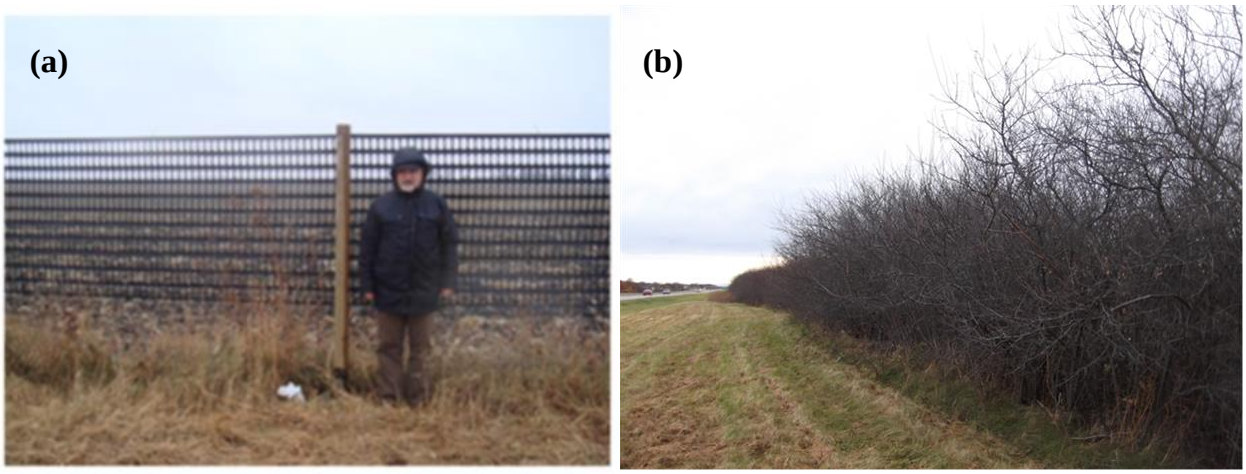

Figure 1 (a) Example of a structural snow fence using lightweight plastic (Basnet et al., 2014). (b) Example of living snow fence in Illinois (photo courtesy of Mark Cornwell).

1.1 Background

Snow fences provide cost-effective, environmentally sustainable solutions to blown snow in the highway environment (Kumar, 2014; Tabler and Meena, 2006). Effective snow fences disrupt air flow causing snow to deposit away from the road (see Figure 2). Snow storage may further increase due to the reduced mobility caused by ice binding. The success of snow fences has been dramatic in many documented cases. For example, installation of snow fences along Interstate 80 in Wyoming reduced accidents by 70% during blown snow events while reducing costs to mitigate blown snow by more than 30% (Tabler and Furnish, 1982). Tabler (2004) also found that pavement protected by snow fences was up to 10°F warmer than unprotected pavement. While these statistics come from sites with structural snow fences, LSFs are anticipated to provide similar or improved benefits.

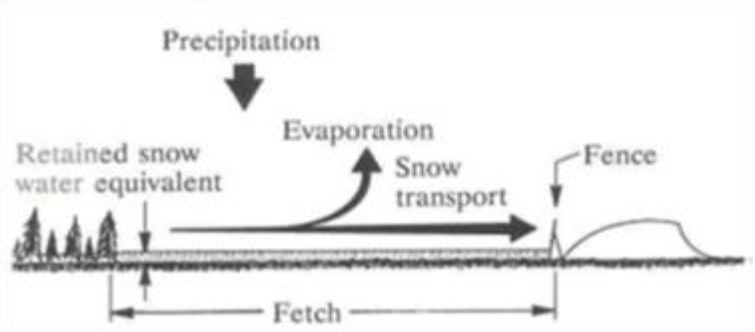

Figure 2 Schematic design of a snow fence (Tabler, 1991).

Designing effective LSFs requires knowledge of the interactions between wind, snow transport and deposition, topography, and snow fences. This problem can be studied in the field, laboratory, or numerically. Field and laboratory approaches may become impractical for design studies due to the high costs and effort required to reproduce the wide range of possible conditions. Such is the case with LSFs, where each fence may be comprised of different types of plant species and placed in a unique topography, prevailing wind conditions, and roadway geometry. An alternative to direct measurements in the field or laboratory is to use numerical simulations. Despite the numerous studies on structural snow fences (Tabler, 2003), research is lacking in the site-specific design of LSFs to reduce the impacts of snowdrifts. Existing design protocols are based on semi-empirical assumptions about snow transport and deposition around structural barriers, which fail to represent the diverse scenarios around LSFs or guide their proper siting and design (Nixon et al., 2006).

Numerical simulation of snow transport around LSFs requires mathematical models describing the aerodynamics, mechanisms of snow erosion and deposition, as well as the influence of the LSF on the flow field. Scale—both spatial and temporal—is an important consideration for these models. In snowdrift applications, models may be continuous—

simulating large areas over an entire snow season—or event-based—simulating a single snow event. Due to the large scales considered, continuous models rely on simplifying assumptions and are often parameterized from field measurements (*e.g.* Walter et al., 2004; Durand et al., 2004; Chen et al., 2009; Grover et al., 2012); whereas, event-based models seek to better capture the underlying physics of the problem and limit parameterization (Uematsu et al., 1991; Xu et al., 2014). Continuous models may not be sufficient for the problem of snow transport around a LSF where small-scale topographic features likely have a significant influence.

Computational fluid dynamics (CFD) has been used to model flow and snow transport around structures including buildings and fences (*e.g.* Uematsu et al., 1991; Sundsbø, 1998; Beyers et al, 2004; Tominaga et al., 2011; Basnet et al., 2014). CFD involves numerical solution of the governing equations of fluid flow, the Navier-Stokes equations, for a given domain geometry and boundary conditions. Amongst the challenges when developing CFD models of LSFs is accurate representation of the fence geometry and topography. The porosity of a fence is an important factor in performance requiring accurate representation for numerical simulations. Prior work has considered manufactured snow fences with regular geometry (Basnet et al., 2014). In this case, fence geometry can be directly incorporated into the numerical mesh. Representing the exact geometry of a living snow fence is not feasible in numerical modeling due to the range of lengths, scales and highly irregular shape of the fence. The difference between fences can be seen by comparing Figure 1a to Figure 1b.

1.2 Objectives

CFD has the potential to provide insight into the mechanisms of aerodynamics and snow transport around snow fences as well as assist in the design of snow fences. Questions remain

regarding the most appropriate techniques required to simulate the aerodynamics around porous fences. This issue is particularly important in the case of LSFs where the complex fence geometry is difficult to represent in a numerical mesh. The objectives of this study are to (1) demonstrate the application of CFD to flow around a porous fence, (2) investigate alternative models for porosity appropriate for LSFs, and (3) quantify the effect of row spacing on aerodynamics around a snow fence.

CHAPTER 2. METHODOLOGY

This report presents results for CFD simulations of flow around porous fences to gain insight into the snow transport process around snow fences. This chapter provides an overview of CFD modeling with emphasis on modeling airflow around porous fences.

2.1 Governing Equations

The flow dynamics of viscous fluids can be described by the equations of mass, momentum, and energy conservation. The energy equation can be neglected for phenomena that can be considered as isothermal. The set of conservation equations consisting of the continuity and momentum equations, which governs the instantaneous viscous fluid motion are often referred to as the Navier-Stokes equations. The Reynolds averaging technique is commonly used to convert the instantaneous components originally included in the Navier-Stokes equations into time-averaged quantities. These time-averaged equations are known as the Reynolds Averaged Navier-Stokes (RANS) equations. For incompressible steady flow, the RANS equations can be formulated into Equations (1) and (2):

$$\frac{\partial U_i}{\partial x_i} = 0 \tag{1}$$

$$U_j \frac{\partial U_i}{\partial x_j} = -\frac{1}{\rho}\frac{\partial P}{\partial x_i} + \nu \frac{\partial^2 U_i}{\partial {x_j}^2} - \frac{\partial}{\partial x_j}(u_i' u_j') + S_i \tag{2}$$

where, P is the mean air pressure, υ is the fluid kinematic viscosity, and S_i represents any source or sink terms added to account for any other external forces, such as gravitational forces. The term x_i refers to the Cartesian coordinates and U_i are the mean fluid velocity components. The term $u_i' u_j'$ are the Reynolds stresses that results from applying the Reynolds averaging. The Reynolds stress is commonly substituted by a function of the mean velocity components by

adopting the concept of the eddy viscosity (ν_t). The eddy viscosity is a numerical parameter in what is commonly referred to as the Boussinesq approximation (Schmitt 2007), which is presented in Equation (3)

$$u_i' u_j' = \nu_t \left(\frac{\partial U_i}{\partial x_j} + \frac{\partial U_j}{\partial x_i} \right) - \frac{2}{3} K \delta_{ij} \quad (3)$$

Where K is the total kinetic energy, ν_t is the turbulent eddy viscosity, and δ_{ij} is the Kronecker delta operator, which equals 1.0 if $i = j$ and 0 otherwise.

2.2 Turbulence Models

The turbulent eddy viscosity (ν_t) needs to be parameterized to close the system of equations. Many closure equations, known as turbulence models, exist with different degrees of complexity and accuracy in replicating features of turbulent flow. The simplest existing turbulence model assumes that ν_t has a constant value over the entire numerical domain. This turbulence model is often referred to as a zero-equation turbulence model; as it does not require solving any additional partial differential equations to estimate ν_t. Other zero-equation turbulence models use algebraic expressions to compute ν_t, such as the mixing length turbulence models. The mixing length concept assumes that ν_t at a certain location is proportional to its distance from a wall, typically the ground boundary condition. Other more sophisticated models use one or more transport equations to estimate ν_t.

The *k*-ε model is one example of a more complex turbulence model that has been used extensively. The *k*-ε model uses two transport equations, one representing the total kinetic energy *k*, and the other representing the energy dissipation rate ε. The computed *k* and ε fields are used to estimate ν_t,

$$\nu_t = C_\mu \frac{k^2}{\varepsilon} \tag{4}$$

where, C_μ is a turbulence correlation constant that is estimated experimentally.

Equations (5) and (6) present the standard *k*-*ε* model developed by Launder & Spalding (1974).

$$\frac{\partial k}{\partial t} + \frac{\partial k U_i}{\partial x_j} = \nu_t \left(\frac{\partial U_i}{\partial x_j} + \frac{\partial U_j}{\partial x_i} \right) \frac{\partial U_i}{\partial x_j} + \frac{\partial}{\partial x_i} \left(\nu + \frac{\nu_t}{\sigma_t} \right) \frac{\partial k}{\partial x_i} - \varepsilon \tag{5}$$

$$\begin{aligned} \frac{\partial \varepsilon}{\partial t} + \frac{\partial \varepsilon U_i}{\partial x_j} &= C_1 \frac{\varepsilon}{k} \nu_t \left(\frac{\partial U_i}{\partial x_j} + \frac{\partial U_j}{\partial x_i} \right) \frac{\partial U_i}{\partial x_j} - C_2 \frac{\varepsilon^2}{k} \\ &+ \frac{\partial}{\partial x_i} \left(\nu + \frac{\nu_t}{\sigma_\varepsilon} \right) \frac{\partial \varepsilon}{\partial x_i} \end{aligned} \tag{6}$$

where C_1, C_2, σ_t, and σ_ε are the model constants with recommended values of 1.44, 1.92, 1.0, and 1.3, respectively. The standard model uses C_μ = 0.09 to compute ν_t from Equation (4). The main advantage of using the standard *k*-*ε* model, compared to the lower order zero and one-equation turbulence models, is its ability to predict both the near-wall and the free-shear flow without any adjustments. Also, it performs better than the lower order models in resolving flows that contain recirculation zones.

One limitation of the standard *k*-*ε* model is that only one turbulence length scale is used in its derivation and therefore the resulting turbulence diffusion only accounts for that length. Yakhot et al. (1992) applied the Renormalization Group (*RNG*) techniques to include many turbulence length scales in the turbulence model. This approach resulted in a new formulation of the energy dissipation equation and generated a new turbulence model, which is known as the *RNG k*-*ε* model. The *RNG k*-*ε* model still uses Equation (4) to compute ν_t with a slightly different value of C_μ equal to 0.085.

Another variation of the *k*-*ε* turbulence model is the Realizable *k*-*ε* model proposed by Shih et al. (1995). This model is called Realizable because the treatment of the Reynolds stresses

is enhanced by satisfying many constraints that result from the turbulence theory. These constraints are not necessarily satisfied by either the standard *k-ε* model and the *RNG k-ε* model. The Realizable *k-ε* model introduces a new formulation of the energy dissipation equation and uses Equation (4) to compute the corresponding ν_t. However, C_μ is no longer a constant and follows a formula that ensures the realizability of the model.

2.3 Numerical Representation of Porosity

Snow fences are obstacles intercepting the air flow and the blowing snow to create a sheltered zone in the leeward side of the snow fence where the air velocity is reduced. The sheltering effect is a result of the snow fence acting as an aerodynamic momentum sink where a proportion of the air momentum is consumed through the drag force applied to the fence and converted to turbulent diffusion (Bourdin & Wilson 2008; Guo & Maghirang 2012). Although solid or relatively dense (low porosity) snow fences lead to a higher reduction in the air speed in the leeward of the fence, they also generate a strong recirculation zone behind the fence and, therefore, lower overall efficiency in promoting snow deposition. As the fence porosity increases, the recirculation zones decreases in size and the sheltering efficiency of the fence decreases (Wang & Takle 1995; Wilson 1985). Wilson (1985) concluded that a fence with porosity ranging from 0.2 to 0.5 will provide the maximum shelter without creating any recirculation zones.

Although porosity is considered a key factor that controls the aerodynamics around the fence, the term porosity may be defined differently depending on the context. One common definition is the optical porosity, defined as the ratio of the frontal projection void area (vertical projection areas where the light can pass through the porous medium) to the total fontal project

area. The optical porosity is often used in designing snow fences, as it is easy to estimate by visual inspection, or by using relatively simple procedures, like photographic optical recognition techniques. Volumetric porosity, on the other hand, is the voids volume not occupied by the solid material normalized by the total porous medium volume. Accurate measurement of the volumetric porosity is quite challenging, especially for complex geometries like those associated with LSFs. Optical porosity works as a good porosity representation in cases of uniform and relatively thin snow fences and, therefore, is suitable to describe structural porous fences. For complex geometries like LSFs, volumetric porosity may perform better than the optical porosity (Rosenfeld et al. 2010). However, Heavey (2013) demonstrated that optical porosity can be used to describe LSFs.

Incorporating the porosity influence in numerical simulations is not straightforward, especially for complex geometries. Therefore, another porosity definition, called the aerodynamic porosity, was introduced that may be a more suitable porosity definition for numerical simulations. The aerodynamic porosity is defined as the ratio of the surface integral of axial velocity component at the downstream edge of the porous medium (U_{x-DS}) divided by the surface integral of the velocities measured far upstream of the fence (U_{x-US}). The aerodynamic porosity definition is represented mathematically in the form presented in Equation (7) (Guan et al. 2003; Rosenfeld et al. 2010).

$$\varphi = \frac{\int_{St} U_{x-DS} dA}{\int_{St} U_{x-US} dA'} \tag{7}$$

where A and A' stand for the fence surface area and the same area located far upstream of the fence, respectively. Note that the aerodynamic porosity is computed from the numerical results itself and therefore avoids any inaccuracies arising from the actual porosity representation in the

model grid or from the constitutive relationships used to account for the influence of the porous medium in the numerical model.

The fence influence on the aerodynamics can be included in numerical models through explicit, semi-implicit, or implicit representations. In explicit representations, like that implemented in Basnet et al. (2014), Endalew et al. (2009) and Alhajraf (2004), the fence geometry is directly represented in the numerical grid. Using this approach requires fine grids and increased computational effort. Therefore, the application of the explicit representation is best suited for fences that have simple regular geometry. The implicit representation, on the other hand, accounts for the pressure drop resulting from the fence in the model by including a sink term in the momentum conservation equation acting on the fence region [term S_i in Equation (2)]. This approach reduces the computational effort required and, therefore, was adopted in the majority of the previous numerical studies to represent both structural and living fences (e.g. Alhajraf 2004; Bitog et al. 2012; Ferreira 2011; Guo & Maghirang 2012; Wilson 1985). Rosenfield et al. (2010) used a semi-implicit fence representation in an attempt to increase the accuracy of the aerodynamics near the fence while keeping the grid size practical. The semi-implicit representation was achieved by explicitly modeling the tree trunks in the model grid as impermeable objects and accounting for the influence of the canopy porosity implicitly in the model. The semi-implicit representation is recommended in 3D simulations where the air can flow around the impermeable trunks. However, this approach is not practical in 2D simulations (Zhou et al. 2002, 2004; Ferreira 2011).

The sink term (S_i) required for the implicit representation can be described using the Darcy-Forchheimer equation

$$S_i = \frac{\Delta P}{\Delta L} = \left(\frac{\upsilon}{K} U_i + \frac{f}{2} U_i |U_i|\right) = \left(\frac{\upsilon}{K} U_i + \frac{k_r}{2\,w} U_i |U_i|\right) \quad (8)$$

where, w is the fence width, K is the fence permeability, and k_r is the pressure loss coefficient, also known as the aerodynamic resistance coefficient. The Darcy-Forchheimer equation estimates the pressure drop as a function of the velocity field at the fence. It consists of the Darcy term ($\frac{\upsilon}{K} U_i$) and the Forchheimer term ($\frac{k_r}{2w} U_i |U_i|$), which account for the viscous and inertial effects, respectively. The viscous effects are important in cases of slow velocity and laminar to low-turbulent flow conditions, and become insignificant when the flow velocity increases, as the inertial effects start to dominate. Therefore, the Darcy term is generally neglected in snow fence simulations, which are typically characterized by highly turbulent flows.

The main difficulty in using the implicit porosity representation is the parameterization of the Forchheimer *f* and the corresponding aerodynamic resistance coefficient k_r. The most accurate way to estimate these parameters is by back calculating from Equation (8) by means of pressure and velocity measurements taken around the fence structure in a controlled wind tunnel experiment. However, the values obtained from wind tunnel experiments cannot be generalized to other fence geometries because the pressure drop resulting from a porous fence depends not only on the fence geometry and porosity but also on the flow field (Hong et al. 2015). Alternative parameterizations have been proposed to estimate k_r. One of the common parameterizations was proposed by Hoerner (1965) to estimate k_r as a function of the fence optical porosity (φ) of a square bar lattices.

$$k_r = \left[\frac{3}{2\varphi} - 1\right]^2 \quad (9)$$

Wilson (1985) used wind tunnel measurements to verify that the Hoerner parameterization gives adequate estimates for a 50% porosity structural fence. Since then, the Hoerner parameterization

has been used in many studies (e.g. Li et al. 2007; Wilson 1985, 1987). Santiago et al. (2007) and Lee & Lim (2001) used a modified parameterization, presented in Equation (10), to correlate the resistance coefficient and the optical porosity with a reported default value of the constant (C_1) equal to 1.04.

$$k_r = C_1 \left[\frac{1-\varphi^2}{\varphi^2}\right] \tag{10}$$

A comparison between the k_r values resulting from Equations (9) and (10) for different optical porosities is presented in **Error! Reference source not found.**3. Differences exist between the k_r values computed using the two parameterizations and become more pronounced at low fence porosities. These differences occur because the resistance coefficient depends on many factors in addition to the porosity including the pore configuration and the obstacle shape. As a result, different fences with the same optical porosity can lead to different resistance coefficients due to the configuration of porous elements and the general fence shape (Wang & Takle 1995).

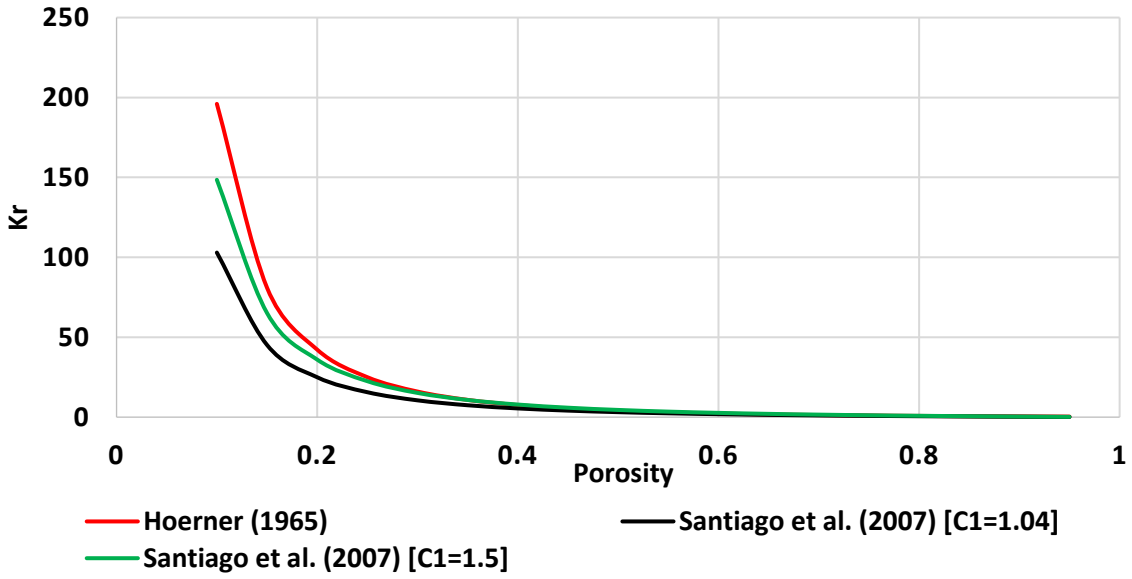

Figure 3 Comparison between the different $\boldsymbol{k_r}$ parameterization for different optical porosities.

In the case of living fences, it is common to estimate the pressure loss as a function of the vegetation geometric and foliage characteristics (Bruse & Fleer 1998; Endalew et al. 2009; Ferreira 2011; Guo & Maghirang 2012) by

$$k_r = 2\int_{-w}^{0} C_d \times SAD\, dx \cong 2\, C_d\, SAD(Z)\, w \qquad (11)$$

where C_d is the drag coefficient and *SAD* is the surface area density, defined as the sum of the vegetative foliage surface area per unit volume (m^{-1}). The drag coefficient typically ranges from 0.1 to 0.5 for most leafed vegetation (Endalew et al. 2009). The SAD can be assumed constant or varying with height according to the vertical distribution of leaves. An *SAD* value of 4.0 is commonly assumed (Ferreira 2011). Tiwary et al. (2005) on the other hand estimated a vertical distribution of *SAD* for three different kinds of vegetation based on their geometric properties. Lin et al. (2007) proposed the following parameterization to account for the vertical variation in the resistance coefficient corresponding to changes in foliage thickness

$$f = \frac{k_r}{w} = \begin{cases} a_1 - \dfrac{a_1 - a_2}{h_1} z & z \le h_1 \\ a_2 - \dfrac{a_2 - a_3}{H - h_1} z & h_1 \le z \le H \end{cases} \tag{12}$$

where, a_1, a_2, and a_3 are constants representing the foliage thicknesses over the vegetation height. Experimental measurements are required to estimate these constants.

Ergun (1952) modified the Darcy-Forchhimer equation to represent the pressure drop that occurs through fluidized beds as a function of the medium porosity producing

$$S_i = \frac{\Delta P}{\Delta L} = \left(\frac{150\mu}{{D_p}^2} \frac{(1-\varphi)^2}{\varphi^3} U_i + \frac{1.75\rho}{D_p} \frac{(1-\varphi)}{\varphi^3} U_i |U_i| \right) \tag{13}$$

where μ is the fluid dynamic viscosity and D_p is the particle diameter of the porous bed. The first term in the right hand side is the Kozeny–Carman equation (Carman 1956), derived from the laminar Hagen–Poiseuille equation by treating the porous medium as a collection of tubular passages. Hence, the application of the Kozeny–Carman equation is restricted to laminar viscous flows. Equation (13) can be used to describe the pressure drop across an LSF by selecting the appropriate particle diameter, or length scale, to represent the LSF canopy structure.

CHAPTER 3. RESULTS

Numerical simulations of flow around porous fences were performed using the computational fluid dynamics software Flow-3D. The experimental data from a wind tunnel study of a non-uniform porous fence was used to validate the modeling approach. Following validation, the numerical approach was used to test a model for fence porosity and investigate the effect of row spacing for fences comprised of two rows of vegetation.

3.1 Model Validation

Living snow fences often have a non-uniform distribution of porosity in the vertical direction. For example, fences comprised primarily of trees may have a region of high porosity near the ground surface (where the solid trunks are spaced intermittently) underneath the lower porosity produced by the dense network of branches and leaves. Experimental data for such cases is limited with an exception being the experiment of Huang et al (2012). In this experiment, vertical velocity profiles around a fence with a non-uniform distribution of porosity were measured in a wind tunnel. The fence height was H = 0.06 m and the top half of the fence was a solid wall (porosity of 0) and the bottom half had a porosity of 0.30. The wind tunnel has dimensions of 0.6 × 0.6 × 8.0 m and is wide enough that wall effect were negligible at the centerline. The uniform inflow velocity was U_o = 10.6 m/s resulting in a Reynolds number of about $R_{eH} = 4.1 \times 10^4$. Huang et al. (2012) report mean streamwise velocity profiles measured with a hot-wire anemometer. Profiles were measured at horizontal locations of x/H = -4, -2, 0, 1, 3, 6, 9, 12, 15, 18, 21, 25, 30 (fence is located at x = 0 m).

To validate the numerical approach, the experimental conditions of Huang et al. (2012) were reproduced and simulated in Flow-3D. The experimental flow conditions can be considered two-dimensional and steady. The numerical flow domain extended a distance of 50H upwind of

the fence and 100*H* downwind of the fence. The height of the flow domain was 10*H*. The bottom boundary was a no-slip wall and the top was a symmetry boundary. The outflow boundary was a pressure boundary and the inflow boundary was a fully developed velocity profile with a mean velocity of 10.6 m/s. Flow domain, geometry, and boundary conditions are illustrated in Figure 4. The flow domain was discretized with a non-uniform Cartesian mesh with a total of 70,278 cells. The near-wall cell size in the vertical direction was selected to produce a y^+-value greater than 30 and less than about 41. A detailed image of the fence geometry and numerical mesh is shown in Figure 5. The simulation was considered converged when the total mass, average mean kinetic energy, average mean turbulent energy, and average mean turbulent dissipation changed by less than 1.0%. This small variation is parameters is indicative of steady-state conditions.

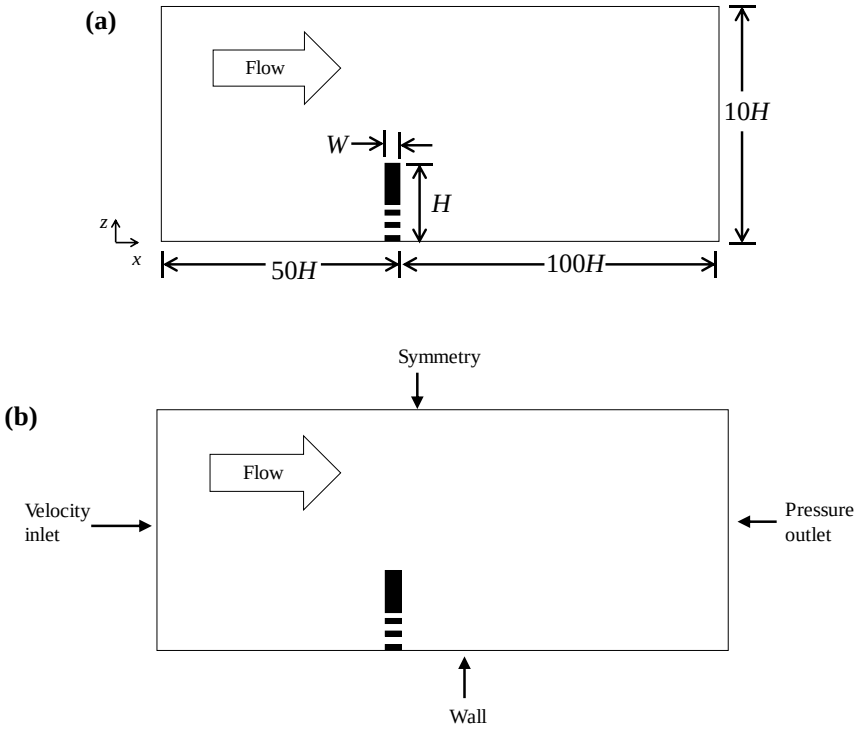

Figure 4 (a) Flow domain and geometry and (b) boundary conditions for simulations based on the experiments of Huang et al. (2012). Drawings not to scale.

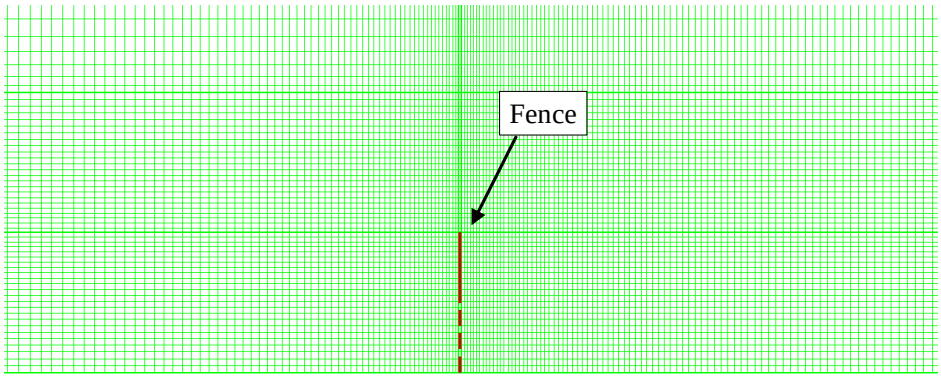

Figure 5 Fence geometry and numerical mesh for simulations based on the experiments of Huang et al. (2012). Flow is from left to right.

The flow field produced by the numerical simulation is shown in Figure 6. Additionally, the flow field resulting from a solid fence with the same geometry and flow conditions is provided. Comparing the two fences demonstrates key features of the porous fence. The flow behind the porous fence is characterized by a region of relatively higher velocity in the lower half of the fence. As a result of this feature, snow is transported through the fence and encounters a low velocity region that causes snow to settle. The absence of this feature in the solid fence means that snow is either deposited on the windward side of the fence or carried over the fence. Once past the fence, the transported snow is located in a region of relatively high velocity, reducing the potential for snow to deposit. Additionally, the velocity above the fence is larger for the solid fence than for the porous fence, indicating a higher capacity to transport snow over the solid fence. A region of low velocity and recirculation forms on the windward side of the solid fence as the wind encounters the impenetrable barrier. While velocity also decreases on the windward side of the porous fence, the velocity decrease is smaller due to the fact the air can pass through the fence.

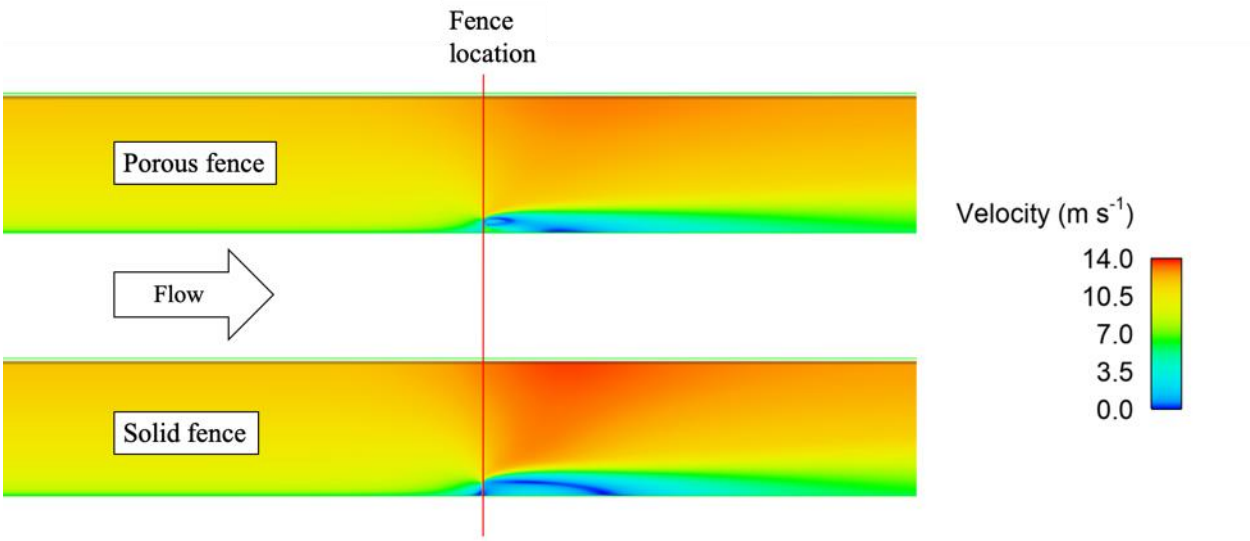

Figure 6 Contours of velocity magnitude from numerical simulations of (a) a fence with non-uniform porosity (top half, $\theta = 0$; bottom half, $\theta = 0.3$) and (b) a solid fence (porosity, $\theta = 0$).

Profiles of the velocity in the *x*-direction, or streamwise velocity, produced by the simulation are compared with the measured values in Figure 7. As with the experiments, the fence is located at $x/H = 0$. Generally, the numerical results are in good agreement with the experiments. Differences are seen in the region close to the fence, for example at locations $x/H = 0$ and 3, below $z/H = 1.0$. Behind the fence is a region of complex flow that is difficult to reproduce numerically and measure experimentally. Despite the difference in magnitude predicted in this area, the qualitative flow pattern is similar. Away from the fence, the numerical solution reproduces the measured profiles well for z/H less than about 2.0. Above this location, the numerical model slightly overestimates the velocity. The region within two fence heights is most important for design and analysis of snow fences. For this reason, the numerical simulation is adequate to reproduce the experimental results and can be used for further investigations of snow fence behavior.

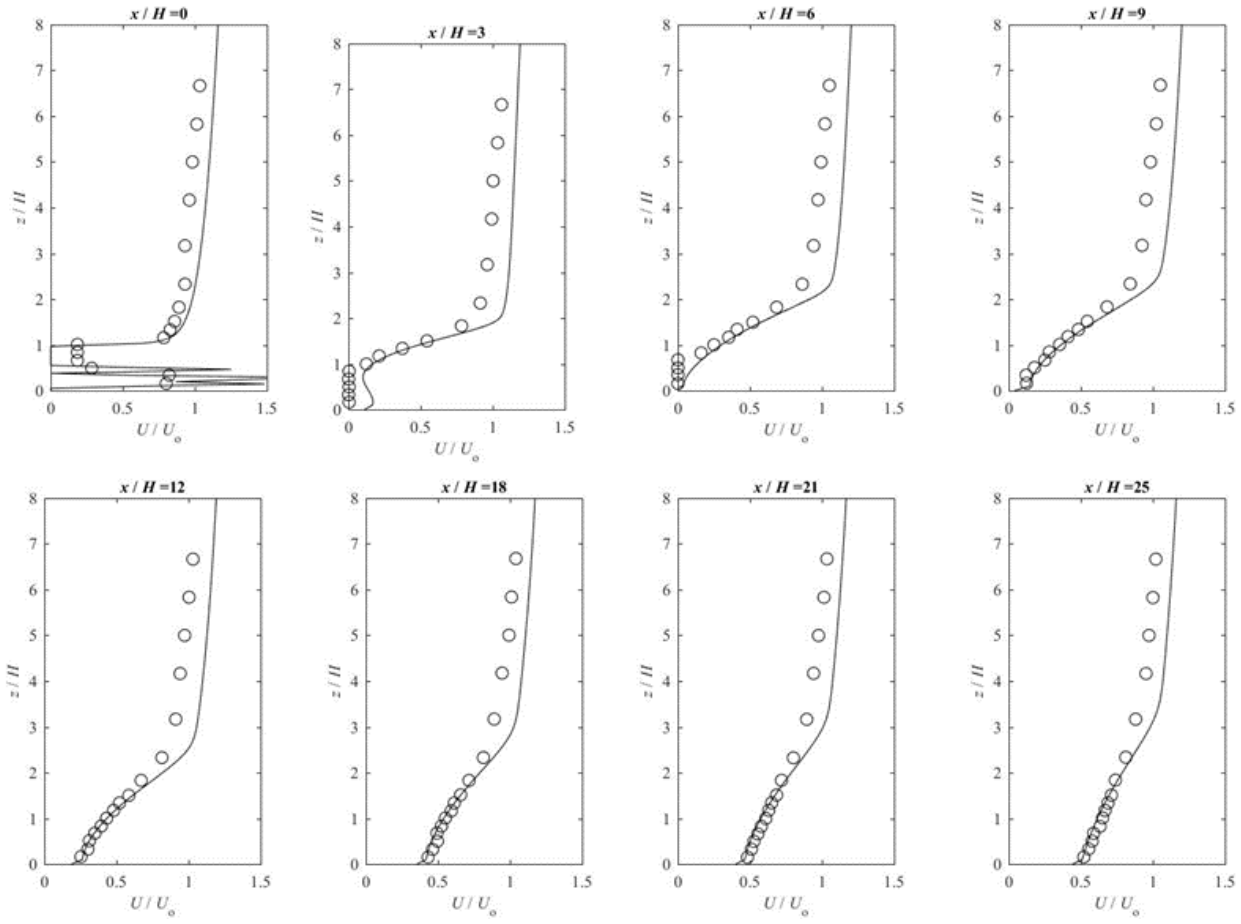

Figure 7 Streamwise velocity profiles from the experimental measurements of Huang et al. (2012) (circles) and numerical simulations (solid lines).

3.2 Porosity Modeling

Representing the true porous fence geometry is difficult for LSFs. The irregular nature of vegetation requires very small cell sizes, increasing computational effort. An alternative approach is to model the bulk effects of porosity on the flow field using the Darcy-Forchheimer equation along with an equation representing the resistance characteristics of the porous fence. To test this approach, a numerical simulation was performed using the Darcy-Forchheimer equation and the Ergun equation for flow resistance. The Ergun equation was developed to

describe flow through a bed of packed spheres. The drag coefficients were determined replacing the sphere diameter with the height of the slats in the porous section of the fence and using the recommended values for the constants, $\alpha = 150$ and $\beta = 1.75$. This approach produced drag coefficients on $A = 3{,}061{,}224$ and $B = 250$. In this simulation, only the representation of the porous portion of the fence changed. The flow domain, fence geometry, mesh, and boundary conditions were identical to the validation case described above.

The contours of velocity magnitude shown in Figure 8 demonstrate that the porosity model reproduces the qualitative flow features of the porous fence. While the horizontal extent of the low velocity region is similar for both approaches, the porosity model produces lower velocity magnitudes in this region. The porosity model also predicts higher velocity magnitudes above the fence. These qualitative observations are confirmed by the velocity profiles. As seen in Figure 9, the porosity model predicts lower velocity behind the fence, *e.g.* at $x/H = 3$, 6, 9, and 12 below $z/H = 2.0$. Additionally, the porosity model slightly over predicts velocity above $z/H = 2.0$ at $x/H = 6$ and 9. As the distance from the fence increases, the two approaches produce essentially the same results. While the porosity model results could be improved by modifying the drag coefficients, the results here demonstrate that the recommended values for the Ergun equation produce reasonable results when compared to both simulations representing the actual porous geometry and measured experimental data.

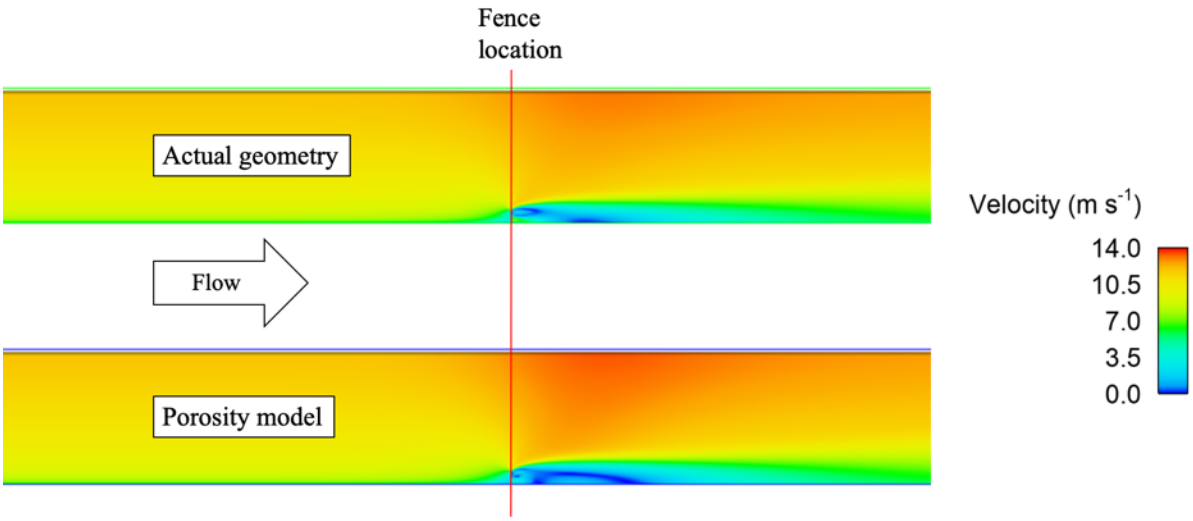

Figure 8 Contours of velocity magnitude from numerical simulations of a fence with non-uniform porosity represent the porosity with the actual geometry and a porosity model.

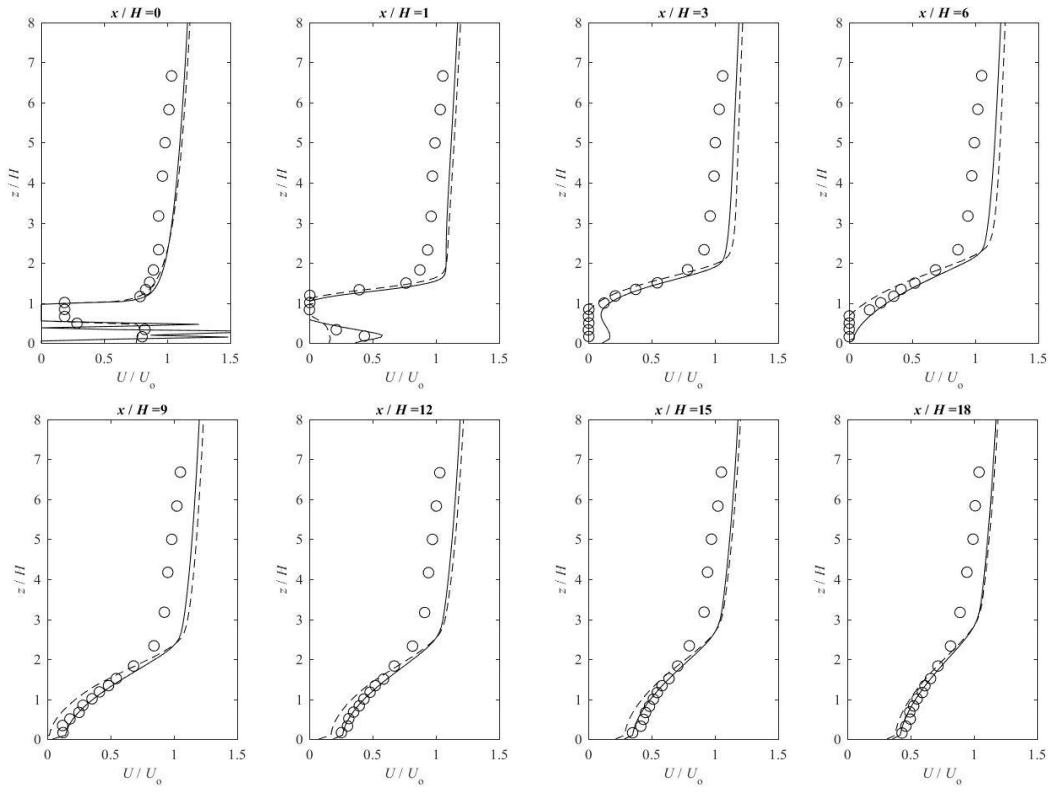

Figure 9 Streamwise velocity profiles from the experimental measurements of Huang et al. (2012) (circles) and numerical simulations representing the actual fence geometry (solid lines) and using a porosity model (dashed lines).

3.3 Influence of Fence Spacing

Vegetation may be planted in rows to form an LSF. To test the effect of row spacing, a series of simulations were performed using two identical fences separated by distances of 0.5*H*, *H*, 2*H*, 3*H*, 5*H* and 10*H*. The geometry of each individual fence was identical to the fence used in the validation simulations based on Huang et al. (2012). The flow domain and boundary conditions were also the same as for the single fence simulations. The mesh was modified to ensure the same distribution of cells around both fences. An example of the two-fence geometry and near-fence meshing is provided in Figure 10.

Contours of velocity magnitude for a single fence and two fences are shown in Figure 11. The flow around two fences is qualitatively similar to flow around a single fence with the addition of a low velocity region in between the two fences. Streamwise velocity profiles for two fences at close spacing (0.5*H*, *H*, 2*H*, and 3*H*) are compared with those for a single fence in Figure 12. In this figure, the x/H-location for the velocity profiles is measured from the second fence in the windward direction. While some differences can be seen, particularly near the fence, the profiles show good agreement. Close to the second fence, the velocity is reduced due to the effect of the first fence, *e.g.*, above $z/H = 1.0$ at $x/H = 0$, 1, and 3. By about $x/H = 6$, the effect of the first fence on the velocity is small and the two fences produce results similar to a single fence. These results confirm prior observations that closely spaced rows of vegetation act essentially as a single fence. When the spacing between fences increases, the first fence exerts a stronger influence on the flow field behind the second fence as demonstrated in Figure 13 for spacings of 5*H* and 10*H*. A greater reduction in velocity is seen above $z/H = 1.0$ near the fence and the influence of this low velocity extends further downwind. At $x/H = 18$, the effects on the

velocity profile are still seen and do not diminish until about x/H = 25~30. Based on these results, fences spaced greater than about 5H should be treated as two individual fences.

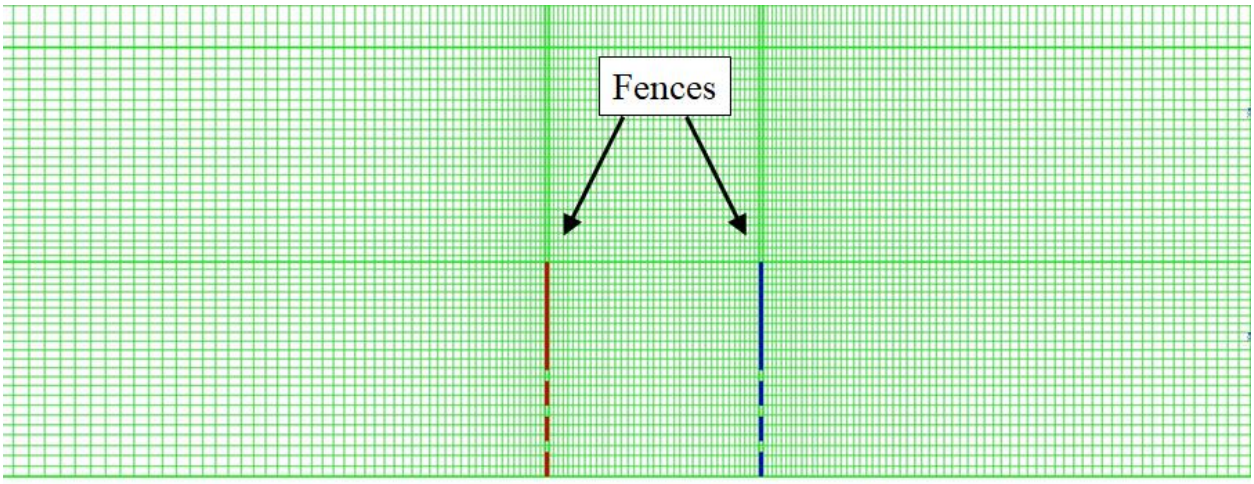

Figure 10 Geometry and numerical mesh for two fences separated by a distance of H. Flow is from left to right.

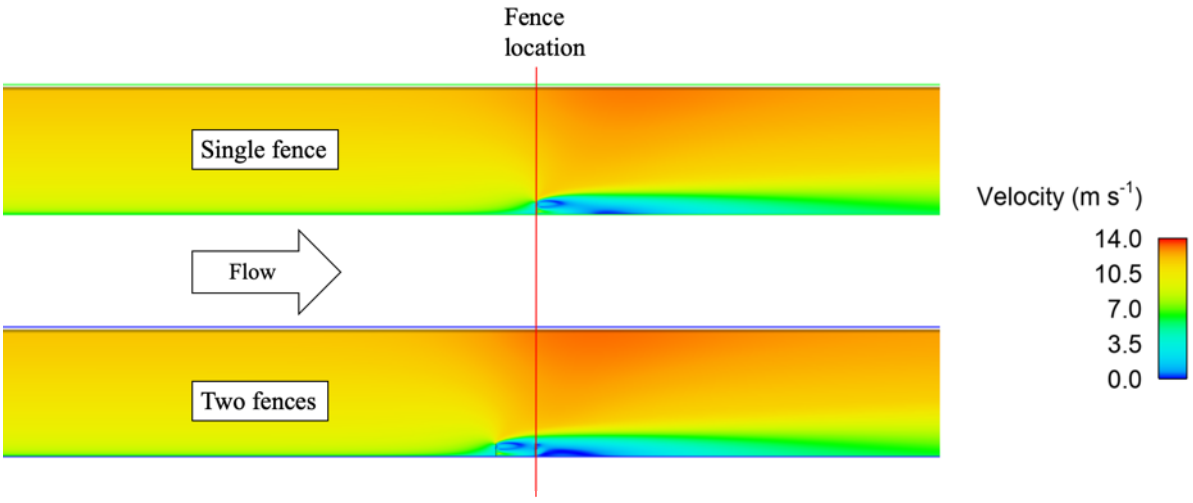

Figure 11 Contours of velocity magnitude around a single fence and two fences separated by a distance of 3H. The red line shows the location of the second fence.

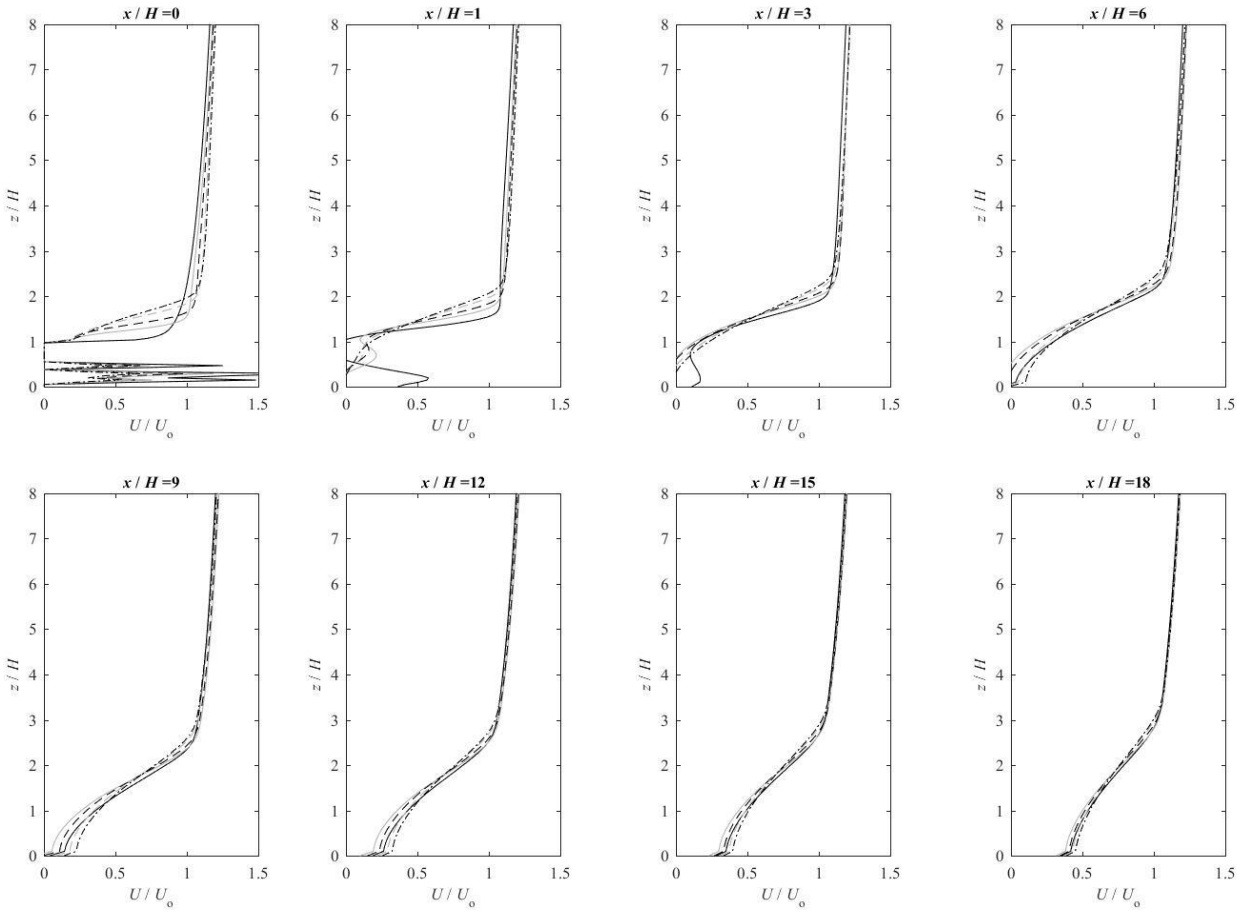

Figure 12 Streamwise velocity profiles behind a single fence (solid black line) and two fences separated by a distance of 0.5*H* (solid grey line), *H* (dashed black line), 2*H* (dashed grey line), and 3*H* (dash-dot black line). For two fences, *x*/*H* specifies the distance behind the second fence.

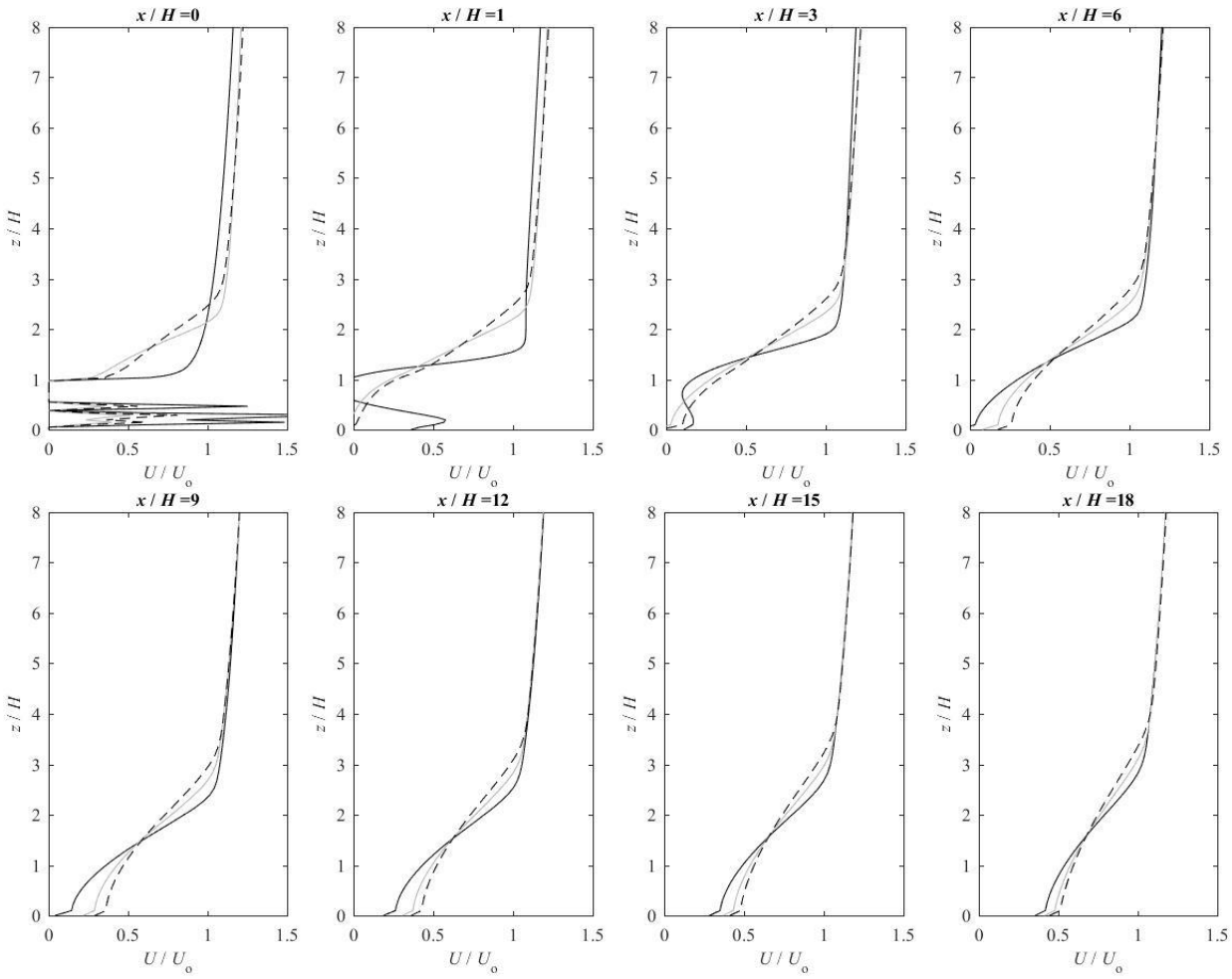

Figure 13 Streamwise velocity profiles behind a single fence (solid black line) and two fences separated by a distance of 5*H* (solid grey line), and 10*H* (dashed black line). For two fences, *x*/*H* specifies the distance behind the second fence.

4. CONCLUSIONS AND RECOMMENDATIONS

The results of this study demonstrate the benefits of simulating aerodynamics around snow fences with CFD. Preliminary numerical simulations reproduced qualitative features of flow around porous fences including a region of reduced velocity on the leeward side of the fence and flow acceleration over the fence. Vertical profiles of streamwise velocity agree well with measured values from the experiment of Huang et al. (2011), particularly in the region below a height of 2*H*. These results demonstrate that CFD simulations can reproduce aerodynamic properties, such as the velocity distribution, around porous fences.

Porosity is a key factor in determining the effectiveness of a snow fence. Two approaches to representing porosity were demonstrated. First, the true fence geometry was directly input into the model as part of the flow domain. The second approach was to model the porosity using the Darcy-Forchheimer equations and the Ergun Equation. In this approach, the fence geometry is represented as if it were a solid object, then the specified porosity and drag coefficients are applied to the fence numerically. The porosity model is advantageous for simulation flow around LSFs due to complex geometry that is difficult to represent directly. Simulation results for the two approaches agree well with some minor differences close to the fence. These results suggest that the porosity model is appropriate to represent the influence of the porous fence on the aerodynamics. Further work is needed to provide recommendations for appropriate use of the Darcy-Forchheimer equation with LSFs. In particular, guidance on the selection of appropriate drag coefficients for different species is needed.

Simulations modeling two porous fences separated by distances up to 10*H* confirm that, for close row spacing (less than about 5*H*), the two fences act similarly to a single fence. This finding has implications for numerical simulations as well as siting of fences. Computational

effort can be reduced when simulating closely spaced fences by including a single composite fence in the flow domain. When designing LSFs, planting a single row of vegetation may be as effective as planting multiple rows so long as the porosity of the single row is similar to the composite porosity of multiple rows. This result is particularly important for sites with small right-of-way where a multi-row fence may not be feasible.

The utility of CFD for design and analysis of snow fences can be enhanced with future work. Topics for further investigation include field data from snow fences as well as incorporating snow transport into the simulations. Monitoring of field sites is needed to provide quantitative data on performance and inform numerical models. The collected data should include, at a minimum, fence geometry and topography, wind speed and direction, as well as measurements of blow snow and snow deposition. Finally, work is needed to incorporate the snow transport process into CFD models. Possible approaches include a Lagrangian particle transport model or an Eulerian multiphase fluid model. These models can be used to correlate snow transport with aerodynamic characteristics to clarify the snow transport and storage mechanisms around porous fences.

REFERENCES

Alhajraf, S. (2004). Computational fluid dynamic modeling of drifting particles at porous fences. *Environ. Model. Softw*. 19, 163–170.

Basnet, K., Constantinescu, G., Muste, M., & Ho, H. (2015). Method to Assess Efficiency and Improve Design of Snow Fences. *J. Eng. Mech*. *141*, 04014136.

Beyers, J.H.M., Sundsbø, P.A., & Harms, T.M. (2004). Numerical simulation of three-dimensional, transient snow drifting around a cube. *J. Wind Eng. Ind. Aerodyn*. 92, 725–747.

Bitog, J.P., Lee, I.-B., Hwang, H.-S., Shin, M.-H., Hong, S.-W., Seo, I.-H., Kwon, K.-S., Mostafa, E., & Pang, Z. (2012). Numerical simulation study of a tree windbreak. *Biosyst. Eng*. *111*, 40–48.

Bourdin, P., & Wilson, J.D. (2008). Windbreak Aerodynamics: Is Computational Fluid Dynamics Reliable? *Bound.-Layer Meteorol*. *126*, 181–208.

Bruse, M., & Fleer, H. (1998). Simulating surface–plant–air interactions inside urban environments with a three dimensional numerical model. *Environ. Model. Softw*. *13*, 373–384.

Carman, P.C. (1956). *Flow of gases through porous media* (Academic press).

Chen, S. S., Lamanna, M. F., Tabler, R. D., & Kaminski, D. F. (2009). Computer-aided design of passive snow control measures. *Transportation Research Record: Journal of the Transportation Research Board*, *2107*, 111-120.

Durand, Y., Guyomarc'h, G., Rindol, L. M., & Corripio, J. G. (2004). Two-dimensional numerical modelling of surface wind velocity and associated snowdrift effects over complex mountainous topography. *Annals of Glaciology*, *38*(1), 59-70.

Endalew, A.M., Hertog, M., Delele, M.A., Baetens, K., Persoons, T., Baelmans, M., Ramon, H., Nicolaï, B.M., & Verboven, P. (2009). CFD modelling and wind tunnel validation of airflow through plant canopies using 3D canopy architecture. *Int. J. Heat Fluid Flow 30*, 356–368.

Ergun, S. (1952). Fluid flow through packed columns. *Chem Eng Prog 48*, 89–94.

Ferreira, A.D. (2011). Structural design of a natural windbreak using computational and experimental modeling. *Environ. Fluid Mech*. *11*, 517–530.

Grover, P., Hellas, N., & McArdle, S. (2012). Snow Transport and Mitigation Modeling System for Managing Snow Drifting Along Highways. *Transportation Research Circular E-C162: Winter Maintenance and Surface Transportation Weather*, 154.

Guan, D., Zhang, Y., & Zhu, T. (2003). A wind-tunnel study of windbreak drag. *Agric. For. Meteorol*. *118*, 75–84.

Guo, L., & Maghirang, R.G. (2012). Numerical simulation of airflow and particle collection by vegetative barriers. *Eng. Appl. Comput. Fluid Mech*. *6*, 110–122.

Heavey, J. P. (2013). *Structure and function of living snow fences in New York State*. State University of New York College of Environmental Science and Forestry, MS Thesis.

Hoerner (1965). *Fluid Dynamic Drag* (Thimphu: Hoerner Fluid Dynamics).

Hong, S.-W., Lee, I.-B., & Seo, I.-H. (2015). Modelling and predicting wind velocity patterns for windbreak fence design. *J. Wind Eng. Ind. Aerodyn*. *142*, 53–64.

Huang, L. M., Chan, M. C., & Lee, J. T. (2012). A Numerical study on flow around nonuniform porous fences. *Journal of Applied Mathematics, 2012*, 12 pp.

Kumar, G. (2014). Performance of snow fence at Banihal top in Himalayan region. *J. Cold Reg. Eng.*, 10.1061/(ASCE)CR.1943-5495.0000088.

Launder, B.E., & Spalding, D.B. (1974). The numerical computation of turbulent flows. *Comput. Methods Appl. Mech. Eng*. *3*, 269–289.

Lee, S.-J., & Lim, H.-C. (2001). A numerical study on flow around a triangular prism located behind a porous fence. *Fluid Dyn. Res*. *28*, 209–221.

Li, W., Wang, F., & Bell, S. (2007). Simulating the sheltering effects of windbreaks in urban outdoor open space. *J. Wind Eng. Ind. Aerodyn*. *95*, 533–549.

Lin, X.-J., Barrington, S., Choinière, D., & Prasher, S. (2007). Simulation of the effect of windbreaks on odour dispersion. *Biosyst. Eng*. *98*, 347–363.

Nixon, W. A., M. Davison, and G. Kochumman (2006). *Living Snow Fences*. Final report for Iowa Highway Research Board Project TR 460, Ames, IA.

Rosenfeld, M., Marom, G., & Bitan, A. (2010). Numerical Simulation of the Airflow Across Trees in a Windbreak. *Bound.-Layer Meteorol*. *135*, 89–107.

Santiago, J.L., Martín, F., Cuerva, A., Bezdenejnykh, N., & Sanz-Andrés, A. (2007). Experimental and numerical study of wind flow behind windbreaks. *Atmos. Environ*. *41*, 6406–6420.

Schmitt, F.G. (2007). About Boussinesq's turbulent viscosity hypothesis: historical remarks and a direct evaluation of its validity. *Comptes Rendus Mécanique 335*, 617–627.

Shih, T.-H., Liou, W.W., Shabbir, A., Yang, Z., & Zhu, J. (1995). A new k-ϵ eddy viscosity model for high reynolds number turbulent flows. *Comput. Fluids 24*, 227–238.

Sundsbø, P. A. (1998). Numerical simulations of wind deflection fins to control snow accumulation in building steps. *Journal of Wind Engineering and Industrial Aerodynamics, 74*, 543-552

Tabler, R. D. (1991). *Snow Fence Guide* (No. SHRP-H-320). Washington, D.C.: Strategic Highway Research Program, National Research Council.

Tabler, R. D. (2003). *Controlling blowing and drifting snow with snow fences and road design*. National Cooperative Highway Research Program Project, (20-7), 147.

Tabler, R. D. (2004). Effect of blowing snow and snow fences on pavement temperature and ice formation. SNOW04-030. *Sixth International Symposium on Snow Removal and Ice Control Technology*. Transportation Research Circular E-C063: Snow and Ice Control Technology. June 2004. pp. 401-413.

Tabler, R. D. and R. P. Furnish (1982). Benefits and costs of snow fences on Wyoming Interstate 80. *Transportation Research Record*, 860, 13-20.

Tabler, R. D., and J. A. Meena (2006). Effects of snow fences on crashes and road closures: A 34-year study on Wyoming interstate-80. *Cold Reg Eng*, 1-10.

Tiwary, A., Morvan, H.P., & Colls, J.J. (2005). Modelling the size-dependent collection efficiency of hedgerows for ambient aerosols. *J. Aerosol Sci*. *37*, 990–1015.

Tominaga, Y., T. Okaze, and A. Mochida (2011). CFD modeling of snowdrift around a building: An overview of models and evaluation of a new approach. *Building and environment*, 46(4), 899-910.

Uematsu, T., Nakata, T., Takeuchi, K., Arisawa, Y., & Kaneda, Y. (1991). Three-dimensional numerical simulation of snowdrift. *Cold regions science and technology*, *20*(1), 65-73.

Walter, M. T., McCool, D. K., King, L. G., Molnau, M., & Campbell, G. S. (2004). Simple snowdrift model for distributed hydrological modeling. *Journal of Hydrologic Engineering, 9*(4), 280-287.

Wang, H., & Takle, E.S. (1995). A numerical simulation of boundary-layer flows near shelterbelts. *Bound.-Layer Meteorol*. *75*, 141–173.

Wilson, J.D. (1985). Numerical studies of flow through a windbreak. *J. Wind Eng. Ind. Aerodyn*. *21*, 119–154.

Wilson, J.D. (1987). On the choice of a windbreak porosity profile. *Bound.-Layer Meteorol*. *38*, 37–49.

Wyatt, G., D. Zomora, D. Smith, et al. (2012). *Economic and Environmental Costs and Benefits of Living Snow Fences: Safety, Mobility, and Transportation Authority Benefits, Farmer Costs, and Carbon Impacts*. Final report for the Minnesota Department of Transportation. MN/RC 2012-03.

Xu, Y., Mustafa, M. Y., & Solvang, W. D. (2014). CFD aided cognitive capabilities for analyzing snowdrift development around a porous fence. In *2014 5th IEEE Conference on Cognitive Infocommunications (CogInfoCom),* Institute of Electrical and Electronics Engineers, 469-473.

Yakhot, V., Orszag, S.A., Thangam, S., Gatski, T.B., & Speziale, C.G. (1992). Development of turbulence models for shear flows by a double expansion technique. *Phys. Fluids Fluid Dyn*. *4*, 1510–1520.

Zhou, X.H., Brandle, J.R., Takle, E.S., & Mize, C.W. (2002). Estimation of the three-dimensional aerodynamic structure of a green ash shelterbelt. *Agric. For. Meteorol*. *111*, 93–108.

Zhou, X.H., Brandle, J.R., Mize, C.W., & Takle, E.S. (2004). Three-dimensional aerodynamic structure of a tree shelterbelt: Definition, characterization and working models. *Agrofor. Syst*. *63*, 133–147.